Giant, 17, 2024, 100235

Full-length article

Structure and transport properties of self-assembled nanofiltration membranes based on sustainably derived materials

Ruiqi Dong, Na Kyung Kim, Chinedum O. Osuji*

Department of Chemical and Biomolecular Engineering, University of Pennsylvania, Philadelphia, PA, 19104, USA

Keywords: self-assembly, nanofiltration, liquid crystal membrane, thin film, sustainable materials

The development of functional polymers using sustainable resources is an increasingly important pursuit. Unsaturated fatty acids represent a potentially interesting class of renewable materials for this purpose. Their unsaturated carbon bonds permit crosslinking to form solid polymers. Additionally, their carboxylic acid functional groups provide for the display of specific surface chemistry within the resulting polymers, and also enable chemical derivatization. Here, we explore the fabrication of nanometer-scale size-selective membranes using conjugated linoleic acid derived monomers. Potassium salt conjugated linoleic acid surfactants (KCLA) self-assembled to form hexagonally packed cylinders (H_I) in an aqueous medium containing glycerol. This structure provides a highly ordered medium with aqueous-continuous channels for nanofiltration. The H_I mesophase was crosslinked with the addition of bifunctional comonomers and the ordered structure was retained with good fidelity in the resulting thin polymer films (< 400 nm thick). These film function effectively as nanofiltration membranes, with a size cut-off of approximately 1.2 nm for charged solutes, while maintaining a high permeance of ~ 9 LMH/bar. This performance is on par with several commercial nanofiltration membranes and these materials are therefore of potential interest for advancing sustainability concerns in practical nanofiltration applications.

Introduction

Chemical separations account for approximately 50% of costs and energy usage in chemical manufacturing [1]. Compared to conventional thermally driven methodologies such as distillation, evaporation, and extraction, membrane-based separation processes often offer the distinct advantages of lower energy consumption and mechanical simplicity [1,2]. The investigation of nanofiltration is driven by the escalating demand for water purification, characterized by increasingly complicated contaminants, including pharmaceuticals, pesticides, industrial chemicals and so on compared to conditions a decade ago. Concomitantly, there is increasing interest in the realization of new improved nanofiltration membranes with pore sizes in the range of 1 to 10 nm [3–5]. Several options are available for nanofiltration membranes currently. These include membranes based on inorganic materials, specifically metal-organic frameworks and zeolites, membranes based on self-assembled block copolymers, those based on polyamide thin-film composites, and membranes made by solvent inversion of polymers such as poly(vinylidene fluoride) (PVDF) and poly(ether sulfone) (PES) [5]. Membranes made using zeolites and frameworks have the advantage of customizable pore sizes and shapes.

* Corresponding author:
E-mail address: cosuji@seas.upenn.edu (C.O. Osuji).

Received 7 November 2023; Received in revised form 29 December 2023; Accepted 29 December 2023

https://doi.org/10.1016/j.giant.2023.100235

This versatility enables the creation of membranes featuring narrow pores (sub-1 nm), and controlled pore-size distribution accompanied by high porosity (~50% or crystal volume) [6,7]. However the inability to produce these materials as large-area defect monolithic films necessitates several compromises in their use in chemical separations, and they are often used as fillers in polymer melts in so-called mixed matrix membranes [8,9]. Furthermore, these materials in the thin-film state are subject to difficult to control intrinsic or extrinsic defects in the grown crystalline domains, resulting in nonselective permeation and posing significant challenges for large-scale reproducible manufacturing [10,11].

An alternative approach involves the use of block copolymers, the self-assembly of which yields membrane materials with well-controlled nanostructure and surface chemistries. Early work by Thomas *et al*. highlighted the potential of block copolymers as nanoporous materials, based on the application of selective etch chemistry [12]. Consistent and scalable processing of block copolymer materials without the need for complex manufacturing techniques is now possible using non-solvent induced phase separation [13–16]. A limitation of block copolymer-based membranes however is the constraint imposed by need for the constituent building blocks to be large enough to drive self-assembly at reasonable temperatures. This manifests itself as a lower bound on the size of pores that can be produced of roughly 5 nm [17,18]. Additionally, the permeability and selectivity of these membranes are compromised by the convolution of the kinetically dictated phase inversion process with thermodynamically driven self-assembly. The result is the production of a more tortuous and less precisely defined transport regulating structure than desired [17–20].

Membranes derived from the self-assembly of polymerizable mesophases of lyotropic liquid crystals (LLCs) provide an attractive option for nanofiltration. The H_I or direct-hexagonal mesophase offers transport in a bicontinuous medium around hexagonally packed cylinders, rather than through discrete cylindrical pores. As a result, the need for orientation control of the structure is obviated and considerations regarding anisotropic transport can be circumvented [21]. Membranes realized by crosslinking H_I mesophases of readily accessible amphiphilic building blocks offer uniform pore sizes that can be precisely specified and varied in the range of ~0.5-2 nm. This is attractive in the context of nanofiltration. [22–25]. At the same time, the transport channels in LLC-derived membranes can be customized based on the headgroup chemistry of the amphiphile, offering the ability to tailor the permeability and selectivity properties of the membranes [26–28]. Consequently, nanofiltration membranes made from LLC mesophases have received increased attention in recent years [29,30].

The development of functional polymers derived from sustainable resources represents an attractive proposition, with economic and environmental benefits relative to traditional petroleum-based materials. This topic is one of increasing concern in the context of materials sustainability [31]. Renewable resources, such as starch, terpenes, cellulose, and natural oils, including octanoic acid, decanoic acid, oleic acid, and linoleic acid, have emerged as candidates of interest in this regard [31–34]. These sustainable resources offer compelling advantages of ready availability, low-cost, and biocompatibility. Especially unsaturated fatty acids, either in their natural or synthetic forms, can be readily chemically derivatized to display diverse surface activities. Moreover, their crosslinkability, stemming from their unsaturated moieties, positions them as potentially important feedstocks in the production of useful polymeric materials [35–37]. Linoleic acid (LA) is one such fatty-acid feedstock, featuring crosslinkable diene groups. The conjugated form, conjugated linoleic acid (CLA), displays better polymerization kinetics than the non-conjugated version, despite the steric constraints originating from the location of the double bonds in the interior of the alkyl tail of the molecule [33].

Here, we explore the use of CLA to create highly ordered nanoporous polymers for use as nanofiltration membranes. The concept is illustrated in Fig. 1. The potassium salt of conjugated linoleic acid surfactants (KCLA) self-assembled as

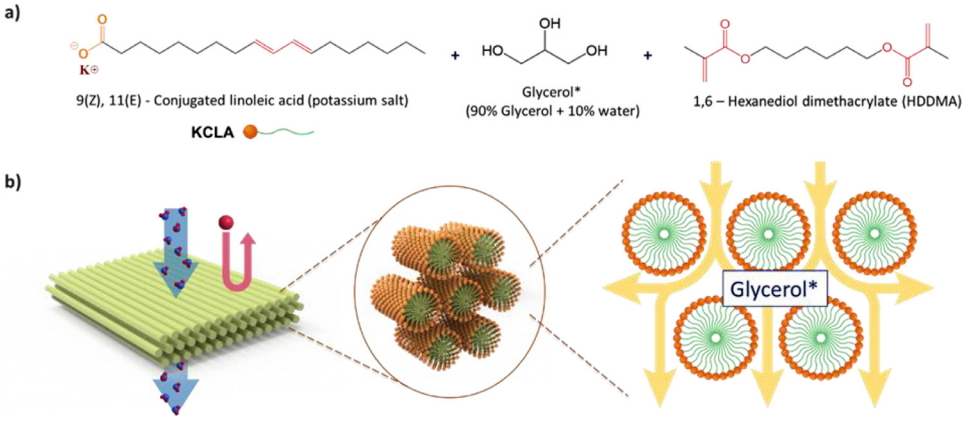

Figure 1

Schematic for fabrication of H_I selective nanofiltration membrane from conjugated linoleic acid-derived system. a) The molecular structure of the lyotropic precursor that self-assembles into the hexagonal mesophase. The mesophase is composed of a polymerizable KCLA, aqueous content glycerol. The HDDMA was added as the crosslinker to help chemically tether the crosslinkable parts. b) Schematic demonstration of the selective separation of the nanoporous features on membrane created by highly ordered packed cylinders.

hexagonally packed cylinders (H_I) in a glycerol-rich aqueous medium (90/10 wt./wt. glycerol/water mixture). The mesophase was crosslinked with methacrylate co-monomers by UV-induced radical polymerization. Thin membranes, ~400 nm thick, were prepared by solution deposition of the mesophase on microporous support membranes, followed by UV-induced crosslinking. These composite thin membranes were deposited on microporous mechanical supports. The composite membrane provided relatively high permeance of ~9 $Lm^{-2}h^{-1}bar^{-1}$, on par with several state-of-the-art commercial nanofiltration membranes (e.g. Dow NF 90). Through conducting a series of pressure-driven solute rejection experiments involving different charged and neutral dyes, the critical effective pore size of these thin membranes is determined ca. 1.2 nm.

Material and Methods

Materials

Octadeca-10, 12-dienoic acid was purchased from Ambeed. Potassium hydroxide, 1,6-hexanediol dimethacrylate (HDDMA), and 2-hydroxy-2-methylpropriophenone (HMP) were purchased from Sigma-Aldrich. Among them, HDDMA was used after the removal of hydroquinone inhibitor by aluminum oxide adsorption. All other chemicals from Fisher Scientific were used without any further treatment.

Synthesis of Potassium Salt Conjugated Linoleic Acid (KCLA) Surfactant

Octadeca-10, 12-dienoic acid and potassium hydroxide were mixed in deionized water at a 1:1 molar ratio. The solution was heated to 55°C and left to react overnight with stirring. The water was removed using lyophilizer to obtain the crude product. The crude product was then further purified by washing with chloroform to eliminate any unreacted octadeca-10, 12-dienoic acid. After drying residual chloroform under vacuum, the resulting KCLA appeared as a white powder. Unlike octadeca-10, 12-dienoic acid, KCLA was soluble in water. The formation of KCLA was confirmed by nuclear magnetic resonance spectroscopy (^{1}H NMR) and Fourier transform infrared spectroscopy (FT-IR). All ^{1}H NMR data was collected by NEO400 with automation using deuterated methanol (MeOD-4) as the solvent and all FT-IR data was collected with FTIR (JASCO 6300) in the attenuated total reflection (ATR) method.

Formation of Lyotropic Liquid Crystal Mesophase

KCLA and aqueous content glycerol (90/10 (w/w) glycerol/water) were mixed at varying weight fractions (0 to 100 wt.%) in centrifuge tubes. The tubes were centrifuged at 14500 rpm for 1 h, followed by manual mixing with blunt needles. These steps were repeated 2-4 times until homogeneous and transparent gels were obtained. The mesophases of mixtures at room temperature were characterized using polarizing optical microscopy (POM) and small-angle X-ray scattering (SAXS). POM images were captured by the Zeiss Axiovert 200M inverted microscope with crossed polarizers. Samples for optical characterization were sandwiched between two glass substrates and thermally annealed with 0.5°C/min to grow larger grains. SAXS measurements were performed using a XAENOCS Xeuss 2.0 system X-ray scattering instruments at the University of Pennsylvania. The instrument was equipped with a GeniX3D Cu beam source with a wavelength of $\lambda = 1.54$ Å. The distance between the detector and samples was calibrated using silver behenate. 2-D scattering plots were integrated into 1-D plots of scattering intensity (I) versus q using Foxtrot software. Each measurement took 10 min to collect enough signals. Unpolymerized sample gels were sealed in quartz capillary tubes, while polymer films and nanoporous membranes were sandwiched between polycarbonate films.

Polymerization of H_I Mesophase

The H_I mesophase formation was observed within the composition between 43 to 65 wt.% KCLA in aqueous content glycerol. To stabilize the H_I mesophase for membrane fabrication, 1,6-hexanediol diamethacrylate (HDDMA) and 2-hydroxy-2-methylpropriophenone (HMP) were added as the co-monomer and photo-initiator. The composition for polymer fabrication was 55/35/9/1 (w/w/w/w) KCLA/Glycerol/HDDMA/HMP with a KCLA concentration of 55 wt.% due to its most ordered structure as indicated by SAXS profiles. The H_I mesophase was fixated by photoinitiated free-radical polymerization, achieved by exposing the mixture under 365nm UV light for 4 h under nitrogen atmosphere. The retention of H_I phases before and after polymerization wasconfirmed by POM and SAXS. The effectivity of crosslinking was assessed by FT-IR.

Fabrication and Characterization of Crosslinked Thin Film

A commercial ultrafiltration membrane made of polyacrylonitrile (PAN, Synder PX) was employed as the mechanical support for the deposition of a hexagonal (H_I) thin film. To create a temporary barrier, a layer of water-soluble polyvinyl alcohol (PVA, MW 13,000-23,000) was applied between the composite membrane and PAN support. 10 wt.% 55 kg/mol PVA was dissolved in water and spin-coated on PAN support at 3000 rpm for 10 min. The membrane casting solution was prepared by dissolving mesophase precursors in methanol at a concentration of 15 wt.%. The solution was filtered through a 0.2 µm polytetrafluoroethylene (PTFE) syringe filter and degassed for 5 min before the usage. The casting solution was then spin-coated on PVA layer at 2000 rpm for 15 min to ensure all solvent evaporated. Subsequently, the film was exposed to 365 nm UV light for 4 h under nitrogen atmosphere for polymerization.

The retention of H_I structure in this thin-film fabrication was determined by POM, SAXS, and grazing incidence small-angel X-ray scattering (GISAXS). For the transmission SAXS characterization, crosslinked spin-coated thin film was scraped from the substrate and subjected to scattering analysis. GISAXS measurements were performed using the same XAENOCS Xeuss 2.0 system X-ray scattering instruments with a GeniX3D Cu beam source with a wavelength of $\lambda = 1.54$ Å. Sample solution was loaded on the pre-cleaned silicon substrates. The silicon substrates were mounted on a standard GISAXS sample holder. The incidence angle between the substrate surface and incoming beam was set as 0.22°. Each measurement took 4 h to collect enough signals. 2-D scattering plots were integrated into 1-D plots of scattering intensity (I) versus q by the Foxtrot software. Casting solutions ranging from 3 wt.% to 20 wt.% were spin-coated on the

silicon substrates following the same polymerization procedure described earlier and then characterized by GISAXS for mesophase retention.

The thickness of thin-film was measured by atomic force microscopy (Bruker Dimension Icon AFM at the tapping mode) and JEOL 7500F field-emission scanning electron microscope (SEM). For AFM measurement, sample solutions were dissolved in methanol and subsequently spin-coated at 2000 rpm onto silicon wafers. Then the spin-coated samples were exposed to ambient air for 5 minutes to ensure complete solvent evaporation prior to photo-crosslinking. After polymerization via UV light exposure, the thin films were scraped a trace of ditch by razor blade for height profile measurement. The height profile of AFM images was analyzed with the software NanoScope Analysis V1.9. The surface morphology and thickness of composite thin film deposited atop PAN were further characterized by SEM. All samples were submerged in a bath of liquid nitrogen until samples became crispy and fractured into 10 mm × 5 mm pieces immediately. For increasing the contrast of these organic samples, before taking the micrograph, the samples were sandwiched between thin specimen split mount and coated with 4nm of Iridium on top of cross-section area. SEM images were photographed with a consistent voltage of 10 kV at a working distance of 10 mm.

Transport Characterization

The crosslinked thin films were cut into circles with a diameter of 4 cm and installed in a 50 mL Milipore Amicon stirred cell (UFSC05001). Supported with a 4.6-cm diameter PE nonwoven mat, the composite membrane was then confined with a customized stainless-steel disk featuring a circular opening area of 0.95 cm^2 for solvent permeation. To investigate the transport properties of this composite membrane, all rejection experiments were driven by compressed nitrogen gas, maintaining a controlled pressure at an average of 35 psi. Magnetic stirring was continued during the whole rejection experiments to avoid concentration gradients. Dye feed solutions were prepared at a concentration of 10 μM in DI water. This is sufficiently low that aggregation of the dye molecules does not occur. All permeates were analyzed by a Cary 300 UV-Vis spectrophotometer.

Results And Discussion

Synthesis of KCLA and Phase Behavior of Lyotropic LC System

The KCLA was readily synthesized by the acid-and-base reaction between octadeca-10, 12-dienoic acid and potassium hydroxide. Note that, compared to salt derived from tung-oil or 10-undecenoic acid, octadeca-10, 12-dienoic acid derived salt has better solubility in aqueous solvent or glycerol. We also found that the synthesized potassium salt CLA (KCLA) demonstrates much better solubility in aqueous solvent than other synthesized alkaline salt forms of CLA, such as NaCLA or LiCLA. The formation of KCLA is confirmed by ^{1}H NMR and FT-IR (**Fig. S1, S2**). On the ^{1}H NMR spectrum, peak b is assigned to the protons adjacent to the carboxylic acid group. The shift in the position of this peak from b to b' signifies the transition from carboxylic acid to carboxylate ion group. On the FT-IR spectrum, the rightward shift of carbonyl stretching vibration of the carboxylic acid (from 1707 to 1560 cm^{-1}) also provides evidence of the formation of carboxylate salt [38]. KCLA is mixed with aqueous content glycerol solution to form lyotropic liquid crystal system. Aqueous content glycerol (90/10 (w/w) glycerol/water) is chosen as the solvent instead of pure water for its higher vapor pressure. This choice facilitates the retention of mesophase geometry during the thin-film fabrication. Within this lyotropic system, the amphiphilic KCLA self-assembles and localizes the ionic head groups exclusively at the hydrophilic/hydrophobic interface, which affords continuous aqueous space and ion-lined domains. As the KCLA concentration increases from 0 to 100 wt.%, mesophase structure transitions from isotropic micellar solution (Iso), hexagonal cylindrical mesophase (H_I), bicontinuous gyroid mesophase (G), to lamellar mesophase (L) (**Fig. S3**). Note that no composition was identified as solely G phase based on the prepared mixtures in the current study. We speculated a pure G phase might appear between 70 to 75 wt.% at room or elevated temperature, within a relatively small window. However, this specific phase was not further investigated in this project. Here we concentrated on the fabrication of membrane with hexagonal (H_I) phase for its larger free-volume fraction and less tortuous pathways compared to other ordered structures, thus leading to higher permeance [2]. While KCLA is a mixture of different isomers, POM and SAXS results are indicative of the formation of a single mesophase, which suggests that the isomers co-assemble, and do not phase separate.

Structural Characterization of Polymer

The formation of an H_I mesophase was observed within the composition range from 43 to 65 wt.% KCLA in the aqueous content containing glycerol. The optimized system was composed of 55/35/9/1 (w/w/w/w) KCLA/Glycerol/HDDMA/HMP. The HDDMA functioned as the crosslinker and HMP as the photo-initiator. The H_I mesophase was fixed by photoinitiated free-radical polymerization with the exposure to 365 nm UV light for 4 h. This amount of crosslinker addition was necessary because the crosslinking of this lyotropic liquid crystal system is subject to the existence of aqueous solvent. Co-monomer HDDMA is slightly soluble in water or glycerol, so the water molecules may encapsulate the KCLA assemblies and prevent the direct contact between KCLA and comonomers, thereby impeding co-polymerization. At the same time, the presence of nucleophilic water tends to terminate the radical chain growth polymerization by capping the carbocation before polymerization can take place [39].

Retention of the hexagonally packed structure of the mesophase after crosslinking was confirmed by POM and SAXS. The typical fan-shaped optical texture, associated with the H_I mesophase, is observed under POM for both mesophase gel before polymerization and the polymer film (Fig. 2a). The bulk film samples for optical characterization were prepared by sandwiching samples between two glass substrates and thermally annealing with 0.5°C/min to grow larger grain size. Also the preservation of H_I mesophase during polymerization is confirmed by the presence of three peaks in SAXS 1D plots with the characteristic d-spacing ratio 1:$\sqrt{3}$:$\sqrt{4}$ corresponding to d_{100}, d_{110}, and d_{200} Bragg peaks (Fig. 2a). Notably the d-spacing shifts from 3.84 to 3.96 nm due to the addition of crosslinkers. The

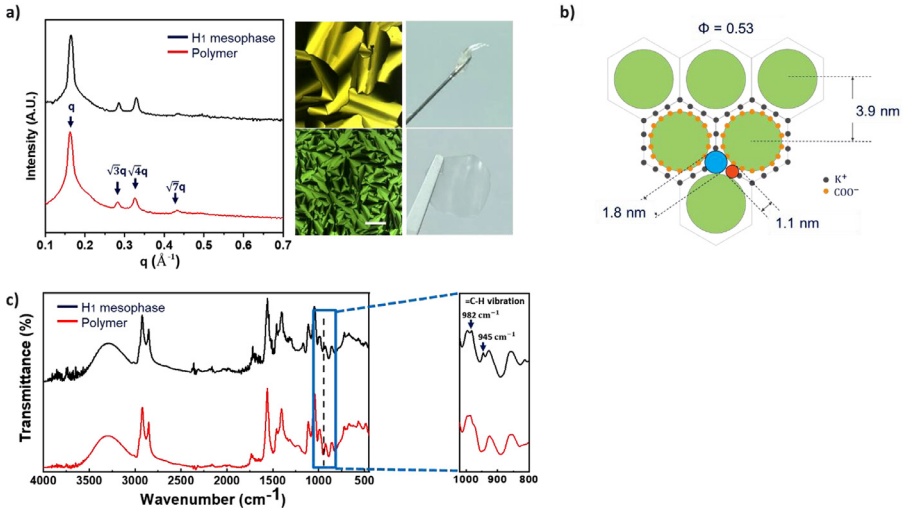

Figure 2

Structural analysis demonstrates the retention of H_I mesophase and polymerization of structures. a) 1D SAXS diffraction data demonstrates the retention of hexagonal mesophase after the addition of crosslinker and polymerization process. POM images of H_I gel (top) and polymer film (bottom) show typical fan-shaped birefringent patterns indicating H_I mesophase. By exposure to UV light, the initial gel-like mixture (top) becomes rigid polymer films (bottom). b) Schematic for an array of hexagonally packed cylinders with water-bicontinuous channels for nanofiltration. Assuming a cylinder volume fraction of 52%, nanochannels provide solute separation size of 1.1 nm scale. c) FT-IR spectra of the HDDMA containing sample before and after photo-polymerization. The window is the zoom-in view of the spectrum between the wavenumber 1000 – 800 cm^{-1}.

effectiveness of polymerization is reflected by the observable transition in appearance from the soft gel to a solid polymer film while preserving optical transparency (Fig. 2a). Fig. 2c displays FTIR spectra that highlights the contrast between the HDDMA containing H_I mesophase before and after UV irradiation. The =C-H vibration bands at 945 cm^{-1} and 982 cm^{-1}, associated with the cis- and trans-diene moieties of the CLAs, undergo a significant reduction, signifying a high conversion rate during the polymerization reaction [22,40]. A conversion rate of 80% is estimated by comparing the characteristic peak areas before and after polymerization. We refrain from using the decrease of C=C vibration at 1653 cm^{-1} as an indicator for the polymerization, as the decrease could originate from the reaction of dienes on both KCLA and crosslinkers HDDMA.

The critical dimensions for solute transport between the hexagonally packed cylinders of the system can be estimated based on the structure characterization data. The volume fraction of the cylinders is corrected from the volume fraction of the KCLA in the system since K^+ is water-soluble. The corrected volume fraction is $\varphi = 0.53$. We calculate the limiting dimensions for transport perpendicular and parallel to the cylinder long axes as 1.07 and 1.77 nm respectively (Fig. 2**b**). These dimensions represent the largest sizes of solute species that could travel unobstructed perpendicular and parallel to the cylinder long axes. A more detailed calculation is shown in ESI. This estimation provides the basis for the subsequent rejection experiments.

Fabrication of H_I Thin-Film Composite Membrane

A schematic illustration of H_I thin-film fabrication process is shown in Fig. 3a. The 55/35/9/1 (w/w/w/w) KCLA/Glycerol/HDDMA /HMP mixture was dissolved in methanol ranging from 3 wt.% to 20 wt.% and subsequently spin-coated at 2000 rpm onto silicon wafers for thickness measurements and structure characterization. Cross-linked thin films were scraped a trace of ditch by blade for preliminary height profile measurement using AFM. A linear correlation between solution concentration and the resulting thickness of the thin film is illustrated in Fig. 3b. Beyond thickness considerations, it is necessary to ascertain the retention of hexagonal structure within spin-coated films. GISAXS was utilized to investigate the preservation of nanostructure in these thin films. After characterizing films deposited from 3 wt.% to 20 wt.% solutions, it is found that the hexagonal mesophase was retained in all samples (Fig. 3c, Fig. S4). Fig. 3c shows an example result of sample deposited from 15 wt.% solution. On 1D plot, three Bragg peaks in the ratio of $1:\sqrt{3}:\sqrt{4}$ correspond to the d_{100}, d_{110}, and d_{200} of the hexagonal mesophase. The primary reflection appeared at a d-spacing of 3.9 nm which is consistent with the result of bulk film. The inset figure exhibits distinct reflection points on the 2D scattering plot. The occurrence of (01) reflection along the specular line indicates that the long axis of the hexagonally packed cylinders resides in the x-y plane of the film. This orientation was not observed in bulk polymer films. The planar orientation of the cylinders is expected in thin films such as those produced by the spin-coating process [25]. Indeed, for transport within discrete cylinders, it is the natural tendency to produce planar cylinders that warrants the use of directed self-assembly approaches to produce vertically aligned cylinders to maximize permeance. Here, due to the transport taking place in the bicontinuous medium surrounding the crosslinked cylinders, there is no such need. Whereas the samples made from lower concentrations like 5 wt.% maintained hexagonal mesophase

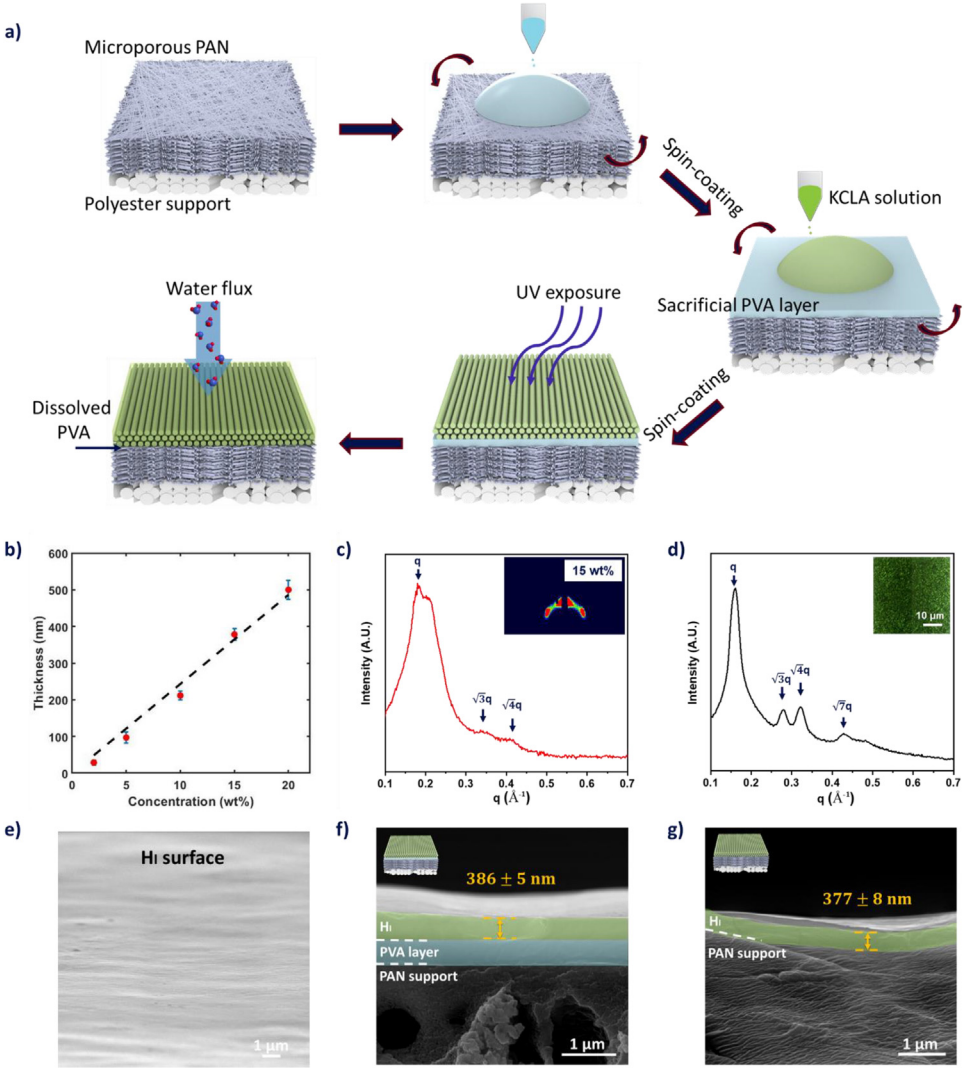

Figure 3

a) Schematic illustration of H_I thin-film fabrication on PAN membrane. H_I solution was spin-coated atop a commercial PAN supports with a sacrificial PVA layer barrier in between. After UV irradiation, the H_I thin film was crosslinked and PVA layer was removed by immersion in water or water flux in the stir cell. b) AFM roughly measured thickness of spin-coated thin film as a function of concentration of mesophase containing solution. The error bar came from at least three measurements. c) GISAXS results of crosslinked thin-film prepared from 15 wt.% solution showed three Bragg spacing d_{100}, d_{110}, and d_{200} in the ratio of 1:$\sqrt{3}$:$\sqrt{4}$ showing on 1D plot and distinct reflection points on 2D plot (inset). d) Mesophase retention in crosslinked thin-film is also proved by characteristic reflection peaks on SAXS plot and typical fan-shaped optical pattern observed in POM image (inset). SEM micrographs for H_I thin-film e) surface and f-g) cross-section. The surface of the thin film after PVA layer removal is significantly smooth. Color overlay is used as a visual aid to delineate the layers. The blue layer represents the PVA sacrificial layer, and the green layer represents the H_I thin film. Before the PVA removal, the thickness of H_I thin film is ~ 390 nm, while the thickness decreases to ~ 380 nm after PVA removal. The decrease might be due to the little infiltration of surface into ultrafiltration membrane during the drying after water immersion.

and offered thinner films with potentially improved permeance, we observed a slight degradation of the hexagonal structure, with the loss of the $\sqrt{4}q$ reflection on SAXS plot, and a rightward shift in all reflections (**Fig. S4**). This nanostructure perturbation may have arisen due to solvent loss during GISAXS scattering and minor uptake of aqueous content from the water-soluble sacrificial layer. Crosslinked spin-coated thin film made with 15 wt.% solution was further characterized by the POM and SAXS. For optical characterization, a casting solution was spin-coated on the glass substrate and slowly thermally annealed following polymerization. A hexagonal phase is confirmed by the fan-shaped optical texture observed under POM and the three Bragg peaks (d_{100}, d_{110}, and d_{200}) occurring in the ratio of 1:$\sqrt{3}$:$\sqrt{4}$ on SAXS 1D plots (Fig. 3d). To satisfy requirements of high permeance and high fidelity of structured geometry, all subsequent thin-film samples were spin-coated from 15 wt.% solutions. Note that the nanostructure within H_I thin-film underwent slight swelling during the filtration experiment. Although direct structural characterization using GISAXS proved challenging with the H_I thin film on the PAN support, indirect structural characterization through humidity-dependent SAXS was conducted on bulk films prepared from this mesophase. The

results indicated the maintenance of the H_I mesophase even as the environmental relative humidity increased from 30% to 90%, with the transport channel expanding by 0.09 nm (13%) due to water uptake.

A commercial microporous membrane served as the mechanical support underlying the thin-film composite membrane in the pressure-driven filtration experiments. To prevent solution infiltration and clogging of the support membrane during the spin-coating process, a previously established sacrificial layer strategy was incorporated into the fabrication procedure [25,26]. The sacrificial layer was introduced between the support and composite film that functioned as a temporary barrier. Polyacrylonitrile (PAN, Snyder PX) has been selected as the commercial microporous support layer owing to its high flow rates and hydrophobicity. 10 wt.% polyvinyl alcohol (PVA) dissolved in water was spin-coated on the surface of PAN membrane at 3000 rpm for 10 minutes to form a smooth sacrificial layer. Then the 15 wt.% composite in methanol solution was spin-coated atop the PVA layer at 2000 rpm for 15 minutes, allowing for complete solvent evaporation. After polymerization, the PVA sacrificial layer was removed by immersing the membrane in deionized water for 2 h. As a result, the selective thin film would lie on the supporting PAN membrane. A schematic illustration of this fabrication process is exhibited in Fig. 3a.

The morphological characteristics and thickness of composite thin-film deposited atop PAN support membrane were assessed using SEM. The micrographs were captured both before and after the removal of the PVA sacrificial layer (Fig. 3e - g). The SEM micrograph of the top-view of thin-film after PVA layer removal shows a considerable smooth surface of spin-coated H_I thin-film (Fig. 3e). The cross-sectional views of the thin-film demonstrate that the H_I layer conformably adheres to the subjacent layer both before and after sacrificial layer removed (Fig. 3f – g). Raw SEM images are shown in Fig. S4d – e. The thickness of the H_I thin film is ~ 390 nm when positioned atop the PVA layer, while thickness displayed a slight reduction to ~ 380 nm after the PVA layer was rinsed away. This reduction in the thickness may be ascribed to minor infiltration of the nanostructure selective layer into the ultrafiltration support membrane during drying after water immersion. It is possible that changes in thickness may also originate due to some swelling or deswelling of the film relative to the conditions under which it was initially characterized. The smooth surface and consistent thickness of H_I thin film substantiate the viability of this thin membrane fabrication process.

Water Permeation and Nanofiltration of Molecular Solutes

The selectivity of the nanoporous membrane was assessed through rejection tests using model penetrant molecules with different sizes. The membrane surface is negatively charged due to the presence of carboxylate groups. To elucidate the selectivity of membrane without the influence of adsorption factors, a series of anionic dyes with sizes ranging from 0.6 nm to 1.8 nm were employed: Methyl Orange (MO), Acid Fuchsin (AF), Reactive Black 5 (RB), Acid Green 1 (AG1), Congo Red (CR), Direct Blue 71 (DR71), and Direct Red 80 (DR80). The molecular dimensions of these dyes were determined by calculating the harmonic mean diameter of dye molecules by equation $d = 3/(d_x^{-1} + d_y^{-1} + d_z^{-1})$, where d_x, d_y, and d_z were estimated based on the simulation calculation using the MM2 energy minimization force field method package in Chem3D software. Detailed molecular structures and sizes of dyes are summarized in **Fig. S5**. The permeates were analyzed by a UV-Vis spectrophotometer. The percentage of rejection was calculated by dividing the permeant concentration by the feed concentration,

$$R = \left(1 - \frac{C_p}{C_f}\right) \times 100\%$$

Fig. 4. reports summarized data derived from the rejection experiments involving all anionic dyes, along with a fitted sigmoidal-like relationship illustrating the solute rejection, R, as a function of solute size, d (Fig. 4b) [41].

$$R_a(\%) = \left(\frac{1}{1 + e^{-\gamma d_s + \beta}}\right) \times 100\%$$

The coefficients γ and β were determined using the least-squares fitting method. With the known γ and β, the critical size d_c corresponding to a 95% rejection rate, was computed. One thing to be noted is that this model was developed to describe the transport between disordered cylindrical packings, as there is currently no published theory available for movement between ordered packed cylinders [42]. All experimental tests were conducted in a 50 mL stirred cell in the laboratory.

H_I thin film was deposited atop a commercial PAN support with a sacrificial PVA layer barrier in between. After the PVA layer was removed, the thickness of the H_1 thin layer is around 380 nm, resulting in a significantly enhanced permeance of ~9 L m^{-2} h^{-1} bar^{-1} and therefore a permeability of ~3 L m^{-2} h^{-1} bar^{-1} μm. The measured permeance and permeability is in close agreement with the estimated theoretical hydraulic permeance and permeability (the detailed calculation is included in ESI).

In addition to its high permeance, this membrane displayed sharp selectivity. Rejection tests with anionic dyes indicated a size cut-off (>95% rejection) for transport at ~1.2 nm, aligning with estimation inferred from SAXS characterization and d_s value simulated using sigmoidal model ($d_s = 1.21\ nm$). Note that to mitigate potential interference from adsorption by the unsaturated H_I membrane or PAN support, the initial 10 g permeate was discarded. Subsequent data were collected after the membrane reached saturation. Measurements were conducted every 3-4 h until dis-negligible permeance increase or rejection failure occurred. Rejection experiments with neutral and cationic dyes were also conducted as supplementary data for membrane's rejection properties (Fig. 4c - d). Among the seven dyes tested, Basic Yellow (BY), Rhodamine 6G (RH6G), Victoria Pure Blue BO (VPB), Tetrazolium Blue (TB), and Alcian Blue 8G (AB8G) are cationic dyes, while Reactive Red 120 (RR120), and Vitamin B12 (VB12) are neutral dyes. The molecular sizes range from 0.9 to 1.7 nm. In these experiments, the initial 15g permeate was discarded, and subsequent data were collected after the membrane reached saturation. The size cut-off was also ~ 1.2 nm. The calculated d_s value from sigmodal model was 1.24 nm, which is also close to the estimation before.

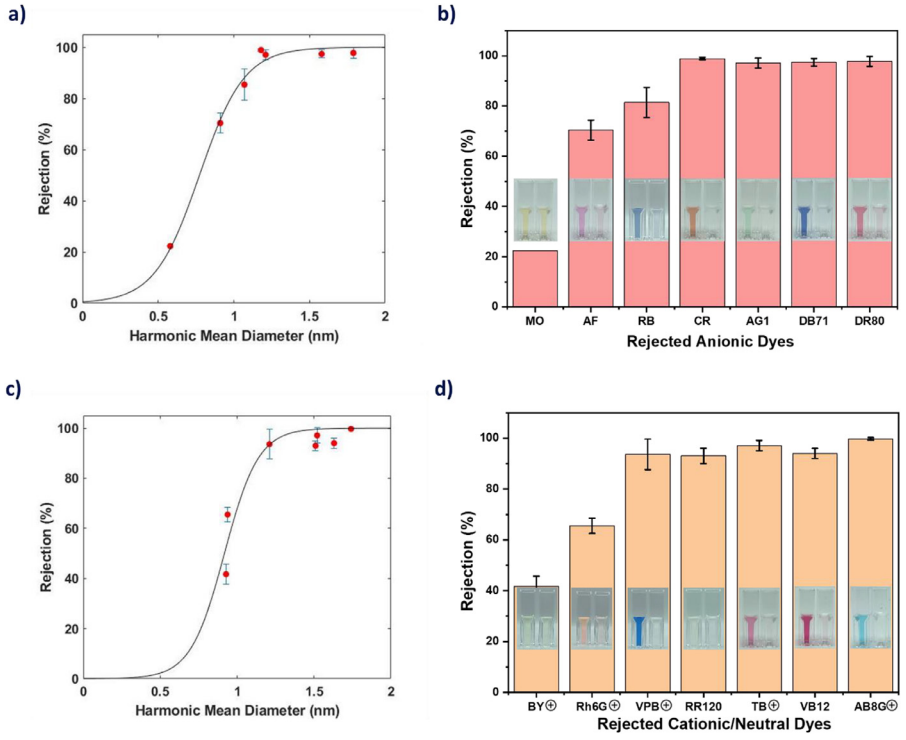

Figure 4

Solute separation performance of the thin lyotropic liquid crystal membranes derived from conjugated linoleic acid. Size-selective solute rejection curves demonstrated the size cut-off of 1.3 nm for a) & b) anionic dye molecules c) & d) cationic / neutral dye molecules. The error bar came from results of three experiments. The cut-off point satisfies the pore size estimation. The insert pictures are photographs of the feed solution versus permeate solution. The PVA supported H_I membrane demonstrates hydraulic permeance 9 LMH/bar.

Conclusion

In conclusion, we developed a direct columnar hexagonal (H_I) mesophase thin membrane that exhibited relatively high permeance and sharp selectivity performance, surpassing existing state-of-the-art commercial membranes. Solute rejection experiments indicated a transport limitation threshold of ~1.2 nm, while maintaining a consistent permeance of ~9 LMH/bar. Additionally, the KCLA membrane was synthesized from the renewable resource conjugated linoleic acid, enhancing its sustainability profile. Noteworthy is the fact that the composite thin membrane comprised only about 10% mass fraction of the commercial microporous membrane support, contributing significantly to sustainability within the engineering process. Prospective investigations could focus on enhancing the robustness of this system by incorporating additional eco-friendly co-monomers to facilitate crosslinking. Exploring the feasibility of generating membranes with adjustable transport channel dimensions by modulating surfactant concentrations within the lyotropic system also holds potential. Another avenue for advancing sustainability could involve the fabricating support membranes utilizing plant-derived materials akin to KCLA.

Declaration of competing interest

The authors declare the following financial interests/personal relationships which may be considered as potential competing interests: Chinedum Osuji reports financial support was provided by National Science Foundation. I am serving as a Guest Editor for the journal. If there are other authors, they declare that they have no known competing financial interests or personal relationships that could have appeared to influence the work reported in this paper.

Data availability

Data will be made available on request.

CRediT authorship contribution statement

Ruiqi Dong: Conceptualization, Data curation, Formal analysis, Investigation, Visualization, Writing – original draft, Writing – review & editing. **Na Kyung Kim:** Data curation, Formal analysis, Writing – review & editing. **Chinedum O. Osuji:** Conceptualization, Formal analysis, Writing – review & editing.

Acknowledgements

This work was supported by NSF through CBET award 2010890. C. O. acknowledges additional support through DMR 2223705. Work was carried out in part at the Singh Center for Nanotechnology which is supported by the NSF NNCI program under grant 2025608, and at the Dual Source and Environmental X-ray scattering facility operated by the Laboratory for Research on the Structure of Matter at the University of Pennsylvania (NSF DMR 2309043). The equipment purchase was made possible by NSF MRI grant (1725969), ARO DURIP grant (W911NF-17-1-0282), and the University of Pennsylvania.

Supplementary materials

Supplementary material associated with this article can be found, in the online version, at doi:10.1016/j.giant.2023.100235.

References

[1] I. Sadeghi, P. Kaner, A. Asatekin, Controlling and Expanding the Selectivity of Filtration Membranes †, Chemistry of Materials 30 (2018) 7328–7354, doi:10.1021/acs.chemmater.8b03334.

[2] J.R. Werber, C.O. Osuji, M. Elimelech, Materials for next-generation desalination and water purification membranes, Nature Reviews Materials, Nature Publishing Group (2016) 1–15.

[3] G. Liu, J. Ding, Diblock thin films with densely hexagonally packed nanochannels, Advanced Materials 10 (1998) 69–71, doi:10.1002/(SICI)1521-4095(199801)10:1⟨69::AID-ADMA69⟩3.0.CO;2-N.

[4] J. Uchida, B. Soberats, M. Gupta, T. Kato, Advanced Functional Liquid Crystals, Advanced Materials (2022).

[5] J. Lugger, D.J. Mulder, R. Sijbesma, A. Schenning, Nanoporous polymers based on liquid crystals, Materials, MDPI AG (2018).

[6] O. Shekhah, J. Liu, R.A. Fischer, C. Wöll, MOF thin films: Existing and future applications, Chemical Society Reviews 40 (2011) 1081–1106, doi:10.1039/c0cs00147c.

[7] J. Cho, Y. Ishida, Macroscopically Oriented Porous Materials with Periodic Ordered Structures: From Zeolites and Metal–Organic Frameworks to Liquid-Crystal-Templated Mesoporous Materials, Advanced Materials, Wiley-VCH Verlag (2017).

[8] F. Cucinotta, Z. Popović, E.A. Weiss, G.M. Whitesides, L. De Cola, Microcontact transfer printing of zeolite monolayers, Advanced Materials 21 (2009) 1142–1145, doi:10.1002/adma.200801751.

[9] M. Ulbricht, Advanced functional polymer membranes, Polymer, Elsevier BV (2006) 2217–2262.

[10] D. Braga, From Amorphous to Crystalline by Design: Bio-Inspired Fabrication of Large Micropatterned Single Crystals, Angewandte Chemie - International Edition (2003) 5544–5546.

[11] E.A. Jackson, M.A. Hillmyer, Nanoporous membranes derived from block copolymers: From drug delivery to water filtration, ACS Nano (2010) 3548–3553.

[12] V.Z.-H. Chan, J. Hoffman, V.Y. Lee, H. Iatrou, A. Avgeropoulos, N. Hadjichristidis, R.D. Miller, E.L. Thomas, Ordered bicontinuous nanoporous and nanorelief ceramic films from self assembling polymer precursors, Science 286 (1999) 1716–1719.

[13] S.P. Nunes, Block copolymer membranes for aqueous solution applications, Macromolecules 49 (2016) 2905–2916.

[14] R.M. Dorin, W.A. Phillip, H. Sai, J. Werner, M. Elimelech, U. Wiesner, Designing block copolymer architectures for targeted membrane performance, Polymer 55 (2014) 347–353.

[15] Y. Zhang, J.L. Sargent, B.W. Boudouris, W.A. Phillip, Nanoporous membranes generated from self-assembled block polymer precursors: Q uo V adis? Journal of Applied Polymer Science 132 (2015).

[16] R.W. Baker, Membrane Technology and Applications, John Wiley & Sons2012.

[17] C. Sinturel, F.S. Bates, M.A. Hillmyer, in: High χ-Low N Block Polymers: How Far Can We Go?, ACS Macro Letters, American Chemical Society, 2015, pp. 1044–1050.

[18] G.M. Geise, D.R. Paul, B.D. Freeman, in: Fundamental water and salt transport properties of polymeric materials, Progress in Polymer Science, Elsevier Ltd, 2014, pp. 1–42.

[19] I.C. Escobar, B. Van Der Bruggen, Microfiltration and ultrafiltration membrane science and technology, Journal of Applied Polymer Science, John Wiley and Sons Inc (2015).

[20] A. Mehta, A.L. Zydney, Permeability and selectivity analysis for ultrafiltration membranes, Journal of Membrane Science 249 (2005) 245–249, doi:10.1016/j.memsci.2004.09.040.

[21] P.W. Majewski, M. Gopinadhan, C.O. Osuji, Understanding anisotropic transport in self-assembled membranes and maximizing ionic conductivity by microstructure alignment, Soft Matter 9 (2013) 7106–7116, doi:10.1039/C3SM50320H.

[22] X. Feng, K. Kawabata, G. Kaufman, M. Elimelech, C.O. Osuji, Highly Selective Vertically Aligned Nanopores in Sustainably Derived Polymer Membranes by Molecular Templating, ACS Nano 11 (2017) 3911–3921, doi:10.1021/acsnano.7b00304.

[23] M. Zhou, T.J. Kidd, R.D. Noble, D.L. Gin, Supported lyotropic liquid-crystal polymer membranes: Promising materials for molecular-size-selective aqueous nanofiltration, Advanced Materials 17 (2005) 1850–1853, doi:10.1002/adma.200500444.

[24] Y. Saadat, O.Q. Imran, C.O. Osuji, R. Foudazi, Lyotropic liquid crystals as templates for advanced materials, Journal of Materials Chemistry A, Royal Society of Chemistry (2021) 21607–21658.

[25] Y. Zhang, R. Dong, U.R. Gabinet, R. Poling-Skutvik, N.K. Kim, C. Lee, O.Q. Imran, X. Feng, C.O. Osuji, Rapid Fabrication by Lyotropic Self-Assembly of Thin Nanofiltration Membranes with Uniform 1 Nanometer Pores, ACS Nano 15 (2021) 8192–8203, doi:10.1021/acsnano.1c00722.

[26] Y. Zhang, D. Kim, R. Dong, X. Feng, C.O. Osuji, Tunable organic solvent nanofiltration in self-assembled membranes at the sub-1 nm scale, Sci. Adv (2022) 5899 -5899.

[27] S. Bhattacharjee, J.A.M. Lugger, R.P. Sijbesma, Tailoring Pore Size and Chemical Interior of near 1 nm Sized Pores in a Nanoporous Polymer Based on a Discotic Liquid Crystal, Macromolecules 50 (2017) 2777–2783, doi:10.1021/acs.macromol.7b00013.

[28] S. Bhattacharjee, J.A.M. Lugger, R.P. Sijbesma, Pore size dependent cation adsorption in a nanoporous polymer film derived from a plastic columnar phase, Chemical Communications 54 (2018) 9521–9524, doi:10.1039/c8cc03292k.

[29] L.N. Bodkin, Z.A. Krajnak, R. Dong, C.O. Osuji, D.L. Gin, Cross-linkable, phosphobetaine-based, zwitterionic amphiphiles that form lyotropic bicontinuous cubic phases, Soft Matter 19 (2023) 3768–3772, doi:10.1039/d3sm00269a.

[30] X. Feng, Q. Imran, Y. Zhang, L. Sixdenier, X. Lu, G. Kaufman, U. Gabinet, K. Kawabata, M. Elimelech, C.O. Osuji, Precise nanofiltration in a fouling-resistant self-assembled membrane with water-continuous transport pathways (2019) 1–11.

[31] Y. Zhu, C. Romain, C.K. Williams, in: Sustainable polymers from renewable resources, Nature, Nature Publishing Group, 2016, pp. 354–362.

[32] T. Jiang, Q. Duan, J. Zhu, H. Liu, L. Yu, in: Starch-based biodegradable materials: Challenges and opportunities, Advanced Industrial and Engineering Polymer Research, KeAi Communications Co., 2020, pp. 8–18.

[33] Y. Fan, Y. Fang, L. Ma, The self-crosslinked ufasome of conjugated linoleic acid: Investigation of morphology, bilayer membrane and stability, Colloids and Surfaces B: Biointerfaces 123 (2014) 8–14, doi:10.1016/j.colsurfb.2014.08.028.

[34] T. Li, C. Chen, A.H. Brozena, J.Y. Zhu, L. Xu, C. Driemeier, J. Dai, O.J. Rojas, A. Isogai, L. Wågberg, L. Hu, Developing fibrillated cellulose as a sustainable technological material, Nature, Nature Research (2021) 47–56.

[35] P.A. Wilbon, F. Chu, C. Tang, Progress in renewable polymers from natural terpenes, terpenoids, and rosin, Macromolecular Rapid Communications (2013) 8–37.

[36] A. Gandini, T.M. Lacerda, A.J.F. Carvalho, E. Trovatti, in: Progress of Polymers from Renewable Resources: Furans, Vegetable Oils, and Polysaccharides, Chemical Reviews, American Chemical Society, 2016, pp. 1637–1669.

[37] M.A.R. Meier, J.O. Metzger, U.S. Schubert, Plant oil renewable resources as green alternatives in polymer science, Chemical Society Reviews 36 (2007) 1788–1802, doi:10.1039/b703294c.

[38] G.M. Bögels, J.A.M. Lugger, O.J.G.M. Goor, R.P. Sijbesma, Size-Selective Binding of Sodium and Potassium Ions in Nanoporous Thin Films of Polymerized Liquid Crystals, Advanced Functional Materials 26 (2016) 8023–8030, doi:10.1002/adfm.201603408.

[39] R.E. Yardley, A.R. Kenaree, E.R. Gillies, Triggering Depolymerization: Progress and Opportunities for Self-Immolative Polymers, Macromolecules, American Chemical Society (2019) 6342–6360.

[40] S. Roberge, M.A. Dubé, Infrared process monitoring of conjugated linoleic acid/styrene/butyl acrylate bulk and emulsion terpolymerization, Journal of Applied Polymer Science 133 (2016), doi:10.1002/app.43574.

[41] Y.-x. Shen, W. Song, D.R. Barden, T. Ren, C. Lang, H. Feroz, C.B. Henderson, P.O. Saboe, D. Tsai, H. Yan, P.J. Butler, G.C. Bazan, W.A. Phillip, R.J. Hickey, P.S. Cremer, H. Vashisth, M. Kumar, Achieving high permeability and enhanced selectivity for Angstrom-scale separations using artificial water channel membranes, Nature Communications 9 (2018) 2294, doi:10.1038/s41467-018-04604-y.

[42] R. Barhate, S. Ramakrishna, Nanofibrous filtering media: Filtration problems and solutions from tiny materials, Journal of Membrane Science 296 (2007) 1–8, doi:10.1016/j.memsci.2007.03.038.